

Imaging the outward motions of clumpy dust clouds around the red supergiant Antares with VLT/VISIR^{*}

K. Ohnaka

Max-Planck-Institut für Radioastronomie, auf dem Hügel 69, 53121 Bonn, Germany
e-mail: kohnaka@mpi.fr.de

Received 27 March 2014 / Accepted 10 June 2014

ABSTRACT

Aims. We present a 0'5-resolution 17.7 μm image of the red supergiant Antares. Our aim is to study the structure of the circumstellar envelope in detail.

Methods. Antares was observed at 17.7 μm with the VLT mid-infrared instrument VISIR. Taking advantage of the BURST mode, in which a large number of short exposure frames are taken, we obtained a diffraction-limited image with a spatial resolution of 0'5.

Results. The VISIR image shows six clumpy dust clouds located at 0'8–1'8 ($43\text{--}96 R_{\star} = 136\text{--}306 \text{ AU}$) away from the star. We also detected compact emission within a radius of 0'5 around the star. Comparison of our VISIR image taken in 2010 and the 20.8 μm image taken in 1998 with the Keck Telescope reveals the outward motions of four dust clumps. The proper motions of these dust clumps (with respect to the central star) amount to 0'2–0'6 in 12 years. This translates into expansion velocities (projected onto the plane of the sky) of 13–40 km s^{-1} with an uncertainty of $\pm 7 \text{ km s}^{-1}$. The inner compact emission seen in the 2010 VISIR image is presumably newly formed dust, because it is not detected in the image taken in 1998. If we assume that the dust is ejected in 1998, the expansion velocity is estimated to be 34 km s^{-1} , in agreement with the velocity of the outward motions of the clumpy dust clouds. The mass of the dust clouds is estimated to be $(3\text{--}6) \times 10^{-9} M_{\odot}$. These values are lower by a factor of 3–7 than the amount of dust ejected in one year estimated from the (gas+dust) mass-loss rate of $2 \times 10^{-6} M_{\odot} \text{ yr}^{-1}$, suggesting that the continuous mass loss is superimposed on the clumpy dust cloud ejection.

Conclusions. The clumpy dust envelope detected in the 17.7 μm diffraction-limited image is similar to the clumpy or asymmetric circumstellar environment of other red supergiants. The velocities of the dust clumps cannot be explained by a simple accelerating outflow, implying the possible random nature of the dust cloud ejection mechanism.

Key words. infrared: stars – techniques: high angular resolution – supergiants – stars: late-type – stars: mass-loss – stars: individual: Antares

1. Introduction

Mass loss is important for understanding the evolution of massive stars. In the red supergiant (RSG) phase, massive stars experience intense mass loss. The RSG mass loss significantly affects the evolution of massive stars, and it is a key to understanding the progenitors of core-collapse supernovae. Nevertheless, the mass-loss mechanism in the RSG phase is a long-standing problem, and the driving force of the RSG mass loss has not been identified yet.

Recent high spatial resolution observations of RSGs have revealed complex asymmetric structures in the region close to the star. The near-IR imaging of the optically bright RSGs Betelgeuse ($\alpha \text{ Ori}$) and Antares ($\alpha \text{ Sco}$) shows asymmetric and clumpy structures (Cruzalèbes et al. 1998; Kervella et al. 2009). In particular, the images of Betelgeuse taken at 1.04–2.17 μm with spatial resolutions of 27–56 mas by Kervella et al. (2009) shows a plume extending to $\sim 130 \text{ mas}$ ($\sim 6 R_{\star}$). Ohnaka et al. (2009; 2011; 2013) carried out high spatial and high spectral resolution observations of Betelgeuse and Antares in the CO first overtone lines near 2.3 μm using the near-IR interferometric instrument AMBER at the Very Large Telescope Interferometer (VLTI). Their “velocity-resolved” aperture-synthesis images revealed temporally variable, inhomogeneous gas motions in the photosphere and the molecular outer atmosphere (so-called

MOLsphere) extending to $\sim 1.5 R_{\star}$. The detected motions are qualitatively similar to the motions of the hotter chromospheric gas spatially resolved by Lobel & Dupree (2001). These observations indicate that the material is not spilling out in an ordered, spherical fashion.

Asymmetric, inhomogeneous structures are also found on larger spatial scales. The near-IR imaging of the dusty RSGs VY CMa and NML Cyg suggests bipolar outflows and/or equatorial disks with even more complex fine structures (e.g. Wittkowski et al. 1998; Kastner & Weintraub 1998; Monnier et al. 2004; Humphreys et al. 2007). Noticeable deviation from spherical symmetry is revealed even in an RSG in an extragalactic system: Ohnaka et al. (2008) spatially resolved the torus around the dusty RSG WOH G64 in the Large Magellanic Cloud using the mid-IR interferometric instrument MIDI at VLTI. Non-spherical mass loss is detected in optically bright (i.e., not very dusty) RSGs as well. The mid-IR imaging of Betelgeuse and Antares by Hinz et al. (1998), Kervella et al. (2011), and Marsh et al. (2001) revealed asymmetric and/or clumpy circumstellar environment extending up to $\sim 100 R_{\star}$. de Wit et al. (2008) detected elongation in the circumstellar envelope of $\mu \text{ Cep}$ at 24.5 μm , which they interpret as the possible evidence of a slowly expanding torus. The 24.5 μm 1D intensity profiles of Antares and $\alpha \text{ Her}$ presented by de Wit et al. (2009) also show extended circumstellar envelopes, although they do not discuss asymmetry. The inhomogeneous gas motions detected in the outer atmosphere might be the seed of the asymmetric and/or clumpy structures seen in the circumstellar envelope.

^{*} Based on VISIR observations made with the Very Large Telescope of the European Southern Observatory. Program ID: 385.D-0120(A), 286.D-5007(A).

Table 1. Summary of the VISIR observations.

Object	UTC	DIT (ms)	NDIT	Seeing (")	Airmass
2010 June 02					
Antares	01:42:59	12.5	24 000	1.2	1.26
	02:09:07	20.0	12 000	1.2	1.17
	02:44:39	20.0	12 000	1.2	1.09
	03:08:37	20.0	12 000	1.2	1.05
	03:31:05	20.0	12 000	1.5	1.03
	03:58:25	20.0	36 000	–	1.01
ϵ Sco	03:41:43	20.0	24 000	1.5	1.05
λ Sgr	02:57:01	20.0	12 000	1.2	1.48
	03:19:55	20.0	12 000	1.2	1.35
2010 November 12 (archived data)					
Aldebaran	07:11:03	12.5	10 240	1.3	1.42

Notes. NDIT: number of frames. Seeing is in the visible.

In this paper, we present $0''.5$ -resolution, diffraction-limited mid-IR imaging of the circumstellar envelope of Antares at $17.7 \mu\text{m}$ with VLT/VISIR. We also report the detection of the outward motions of clumpy dust clouds over 12 years. Antares (M1.5Iab-b) is a well-studied prototypical RSG at a distance of 170 pc (based on the parallax from van Leeuwen 2007) with a moderate mass-loss rate of $\sim 2 \times 10^{-6} M_{\odot} \text{yr}^{-1}$ (Braun et al. 2012). From its effective temperature (3660 ± 120 K) and luminosity ($\log L_{\star}/L_{\odot} = 4.88 \pm 0.23$), its mass is estimated to be $15 \pm 5 M_{\odot}$ (Ohnaka et al. 2013). Antares has a hot companion (B2.5V) at a separation of $2''.7$, which can be used to probe the mass loss from the primary RSG (e.g., Baade & Reimers 2007; Reimers et al. 2008).

2. Observations and data reduction

2.1. VISIR observations

We observed Antares with VLT/VISIR (Lagage et al. 2004) on 2010 June 2 (UTC) using the Q1 filter centered at $17.7 \mu\text{m}$ with a half-band width of $0.83 \mu\text{m}$. VISIR is equipped with a 256×256 BIB detector with pixel scales of $0''.075$ and $0''.127$. We used the pixel scale of $0''.075$ for our observations of Antares. The observations were carried out with chopping and nodding to subtract the sky background. We used a chopping and nodding angle of $8''$ with the direction of the chopping and nodding set to be perpendicular. This results in four images on the detector after processing the chopped and nodded frames. The chopping frequency was 0.5 Hz, and the nodding period was 90 s.

We took advantage of BURST mode (Doucet et al. 2007), which takes a number of exposures with a short detector integration time (DIT) to freeze the atmospheric turbulence. This allows us to obtain a diffraction-limited image, which is difficult to achieve in normal long exposures (see, e.g., Kervella & Domiciano de Souza 2007 for comparison of the images taken in BURST mode and usual long-exposure mode). As Table 1 summarizes, we took 108 000 frames for Antares and 24 000 frames for the calibrators ϵ Sco and λ Sgr, using DITs of 12.5 and 20 ms.

We observed these calibrators not only for the flux calibration of the Antares image but also as references of the point spread function (PSF). However, as we present below, while the Antares image shows up to the tenth Airy ring, we detected only up to the third Airy ring in the image of ϵ Sco and only the central core in the image of λ Sgr, because these calibrators

are much fainter than Antares¹. This makes the quality of the PSF-subtracted image of Antares remarkably worse than before the PSF subtraction. Therefore, as a second PSF reference, we downloaded archived VISIR BURST mode imaging data of Aldebaran (α Tau) taken on 2010 November 12 with the Q1 filter (Program ID: 286.D-5007A, published in Kervella et al. 2011) and reduced them in the same manner as our data.

2.2. Data reduction

The data reduction of the BURST mode data is as follows. We first removed the sky background by subtracting the chopped and nodded images. Since the chopping and nodding direction are perpendicular to each other, we obtain four images after this procedure. However, in the data of Antares, one of the four images falls onto a region significantly affected by a group of bad pixels, and it must be discarded. In addition, as Fig. 1a shows, the images after the chopping and nodding subtraction show noticeable horizontal stripes, which are reported by Kervella et al. (2011). The horizontal stripes are not fixed to specific rows but appear in different rows in each frame. To remove these detector artefacts, we applied the following method presented by Kervella et al. (2011) to each image after the chopping and nodding subtraction. At each row, we computed the median in 20 pixels from the left (right) edge of the image and subtracted it from the left (right) half of the image. This procedure mostly removes the horizontal stripes, as Fig. 1b shows. Then we recentered each image and added all images to obtain the final images of Antares and the calibrators with IRAF².

However, the shift-and-added images still show some residual of the horizontal stripes, which appears as a regular vertical pattern in columns near the center (Fig. 1c). The amplitude of the vertical pattern is $\sim 0.2\%$ of the peak intensity of the central star in case of Antares. While this appears to be small, we attempted to remove the artefact to minimize its effects on the study of the faint circumstellar structures. The vertical pattern appeared in the shift-and-added images of Antares and Aldebaran but not in the images of the calibrators ϵ Sco and λ Sgr, which are much fainter than the former two stars. To remove this artefact, we fitted it with a sinusoidal curve outside the region dominated by the bright central core of the image. Specifically, to remove only the artefact while leaving the Airy pattern intact, we first estimated the Airy pattern in the affected central 15 columns by interpolating from the adjacent pixels and subtracted the interpolated Airy pattern in each column. The remaining artefact was fitted with a sinusoidal function in each column in the region outside the bright Airy rings (outside the fifth and third Airy rings for Antares and Aldebaran, respectively. See also Fig. 2 and 4c). The fitted sinusoidal pattern was subtracted for all pixels (i.e., also for pixels excluded from the sinusoidal fitting) in each column. The resulting image (Fig. 1d) shows that the vertical pattern is mostly removed.

2.3. Flux calibration

We carried out the flux calibration of the image of Antares using the calibrators ϵ Sco and λ Sgr. We adopted the Q1-band flux of 18.59 Jy and 9.9 Jy for ϵ Sco and λ Sgr, respectively, taken

¹ No brighter calibrators could be observed because the telescope had to be closed due to strong winds.

² IRAF is distributed by the National Optical Astronomy Observatory, which is operated by the Association of Universities for Research in Astronomy (AURA) under cooperative agreement with the National Science Foundation.

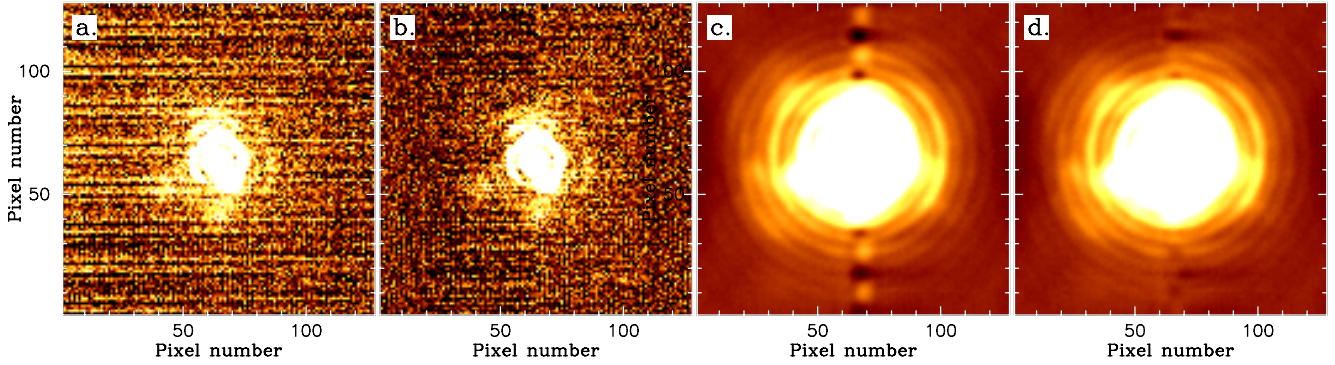


Fig. 1. Removal of the detector artefacts. **a)** One of the chop-nod processed images of Antares, showing horizontal stripes. **b)** Same image as in **a)**, after the removal of the horizontal stripes, as described in Sect. 2.2. **c)** Shift-and-added image of Antares obtained from all frames, in which the horizontal stripes are removed. The image shows an artefact that appears as the vertical regular pattern, whose amplitude is $\sim 0.2\%$ of the peak intensity of the central star. **d)** Same image as in **c)**, after removing the vertical pattern, as described in Sect. 2.2.

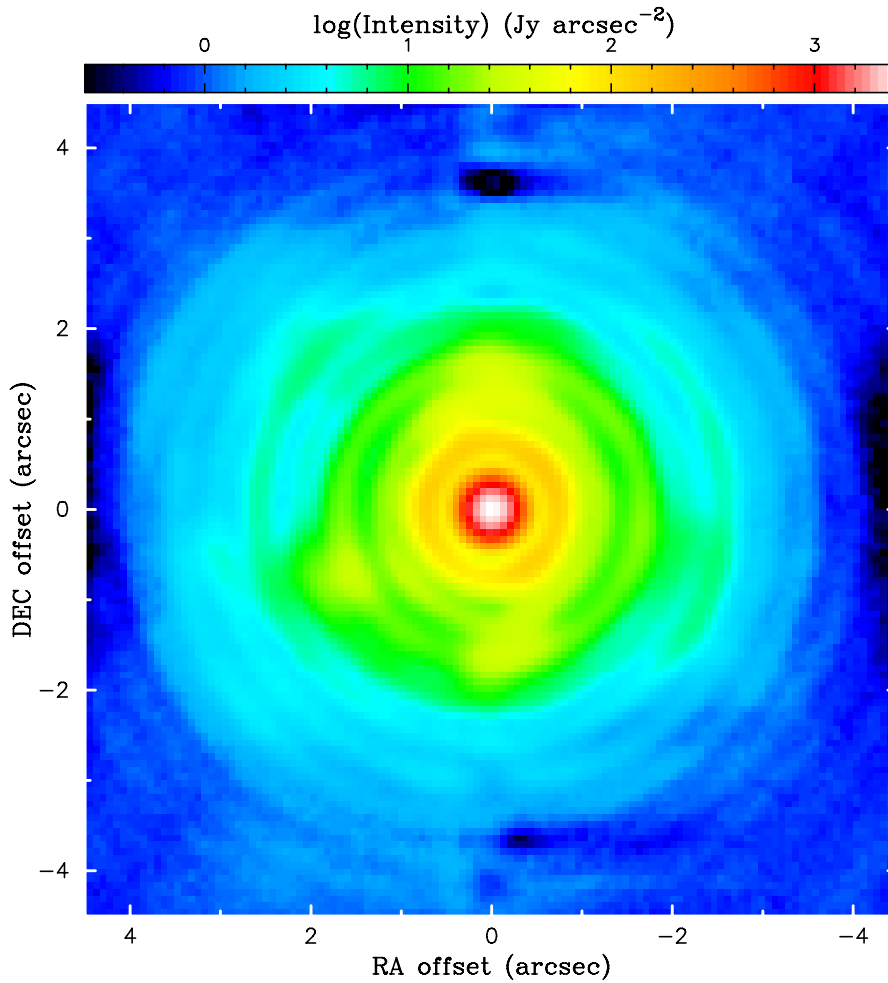


Fig. 2. Flux-calibrated $17.7 \mu\text{m}$ image of Antares. The colors are shown on a logarithmic scale. North is up, and east to the left.

from the catalog of the mid-IR standard stars on the VISIR website³. The $17.7 \mu\text{m}$ flux of Antares calibrated with ϵ Sco and λ Sgr is 1135 Jy and 1282 Jy, respectively. With λ Sgr much fainter than ϵ Sco, the image quality of λ Sgr is very poor, making the flux obtained with this calibrator less reliable than obtained with ϵ Sco. Therefore, we take the value derived with ϵ Sco as the flux of Antares and the difference in the flux derived with ϵ Sco and λ Sgr as the uncertainty in the flux calibration (1135 ± 148 Jy). The flux derived from the spectrum obtained

with the Infrared Space Observatory (TDT number: 08200369) and the response function of the Q1 filter⁴ is 1224 Jy, which agrees with the 1135 ± 148 Jy obtained above within the error.

3. Results

Figure 2 shows the flux-calibrated $17.7 \mu\text{m}$ image of Antares. The high brightness of Antares and the BURST mode allowed us to detect up to the tenth Airy ring, which is clearly seen

³ http://www.eso.org/sci/facilities/paranal/instruments/visir/tools/zerop_cohen_Jy.txt

⁴ http://www.eso.org/sci/facilities/paranal/instruments/visir/inst/Q1_rebin.txt

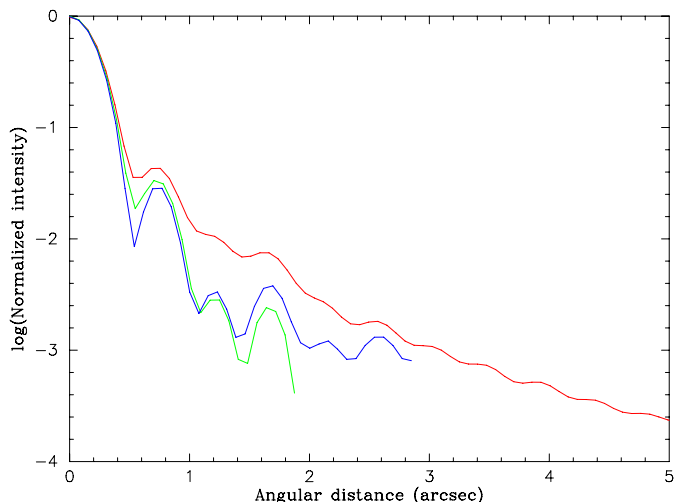


Fig. 3. Azimuthally averaged intensity profiles of Antares (red), ε Sco (green), and Aldebaran (blue). The intensity profiles are normalized with the peak intensity.

in the azimuthally averaged intensity profile shown in Fig. 3. Comparison of the intensity profile of Antares with those of ε Sco and Aldebaran reveals the extended circumstellar envelope. We also show an enlarged view of the inner $3'' \times 3''$ region of the Antares image and the images of the PSF references ε Sco and Aldebaran in Fig. 4. The central core of the image of ε Sco (Fig. 4b), which was observed on the same night as Antares, has a FWHM of $0''.5$, which corresponds to the diffraction limit of VLT at $17.7 \mu\text{m}$. The peak intensity of the Antares image is $2616 \text{ Jy arcsec}^{-2}$. Figure 2 reveals three clumpy features at $1''.5$ in the north and south and $1''.8$ in the southeast. Figure 4a shows the same image on a different color scale, where these features are easier to recognize. The clumpy features are not present in the image of ε Sco (Fig. 4b), where up to the third Airy ring is detected. The upper right corner of the ε Sco image is masked because of strong residuals of a detector artefact. However, the image quality of ε Sco is much worse than Antares. Therefore, we checked further whether the clumpy features are real or not, using the image of the second PSF reference Aldebaran. While Aldebaran was observed on a totally different night from Antares, the difference between the image of ε Sco and Aldebaran is 2.5% at most, as shown in Fig. 4d, suggesting that the PSF is stable. The image of Aldebaran (Fig. 4c) shows up to the fifth Airy ring. Although the fourth and fifth rings are noisy (the fourth ring is barely visible), there is no signature of the clumpy features. Therefore, the clumpy features in Antares are not PSF artefacts but real.

We checked whether the residual of 2.5% between the PSFs from ε Sco and Aldebaran can be explained by the difference in the orientation of the pupil with respect to the field of view. However, we confirmed that this cannot explain the difference in two PSFs. The residual of two PSFs may result from a slight difference in the telescope optics between the observations of ε Sco and Aldebaran.

To better study the clumpy structures, we need to remove the Airy pattern resulting from the unresolved central star. However, there is also emission from the circumstellar envelope in front of the star. To remove only the unresolved central star while leaving the emission from the circumstellar envelope intact, it is necessary to estimate the flux contribution of the central star at $17.7 \mu\text{m}$. In previous studies, difference methods were taken to this end. For Antares, Marsh et al. (2001) derived a maximum

likelihood solution with the flux contribution of the central star and the (positive) background treated as unknowns. As they note, this corresponds to subtracting the largest contribution of the central star without introducing significant negative residuals in the PSF-subtracted image. For the mid-IR imaging of Betelgeuse, Kervella et al. (2011) estimate the flux contribution of the central star using the spectral energy distributions (SEDs) predicted by model atmospheres.

We took a different, “interferometric” approach by computing the visibility, which is the amplitude (i.e., modulus) of the complex Fourier transform of the object’s intensity distribution in the sky. We computed the Fourier transform of the images of Antares and the calibrator ε Sco and obtained the calibrated visibility of Antares by dividing the (raw) visibility of Antares with that of ε Sco. The calibrated 2D visibility of Antares, shown in Fig. 5a, is characterized by a sharp drop at low spatial frequencies (corresponding to the extended component) and a plateau at high spatial frequencies (corresponding to the unresolved component), which is clearly seen in the azimuthally averaged visibility (Fig. 5b). This is typical of an object consisting of an unresolved central source and a well resolved extended component. The visibility of the plateau region corresponds to the fractional flux contribution of the unresolved central star. We adopted the average of the visibility between a spatial frequency of 1.0 and 1.9 arcsec^{-1} , 0.633 , as the fractional flux contribution of the central star. The flux contribution of the central star is $1135 \times 0.633 = 718 \text{ Jy}$.

The image of the calibrator ε Sco was scaled to match this flux of the central star of Antares, and the flux-scaled PSF was subtracted from the flux-calibrated image of Antares. We generated a flux-scaled PSF from the Aldebaran data as well. For a better registration of the Antares and calibrator images, the images were resampled by a factor of 4 using 2D spline interpolation before the subtraction, and the PSF-subtracted images were then binned back with four pixels.

Figure 6 shows the PSF-subtracted image of Antares obtained with ε Sco (Fig. 6a) and Aldebaran (Fig. 6b). While the quality of the PSF-subtracted image with ε Sco is not very good, three clumpy structures seen in Fig. 2 can be recognized. They appear more clearly in the PSF-subtracted image obtained with Aldebaran. The PSF-subtracted images reveal two additional clumps west and southwest of the star (C and D) at a distance of $0''.8$. We also detected compact emission at the center with a radius of $0''.5$. The central compact emission in the PSF-subtracted image with Aldebaran is double-peaked, while it is single-peaked in the image obtained with ε Sco. As we discuss below, this results from the uncertainty in the PSF, and therefore, the double peak in Fig. 6b cannot be confirmed to be real. The radius and position angle of the clumps are listed in Table 2. We split the northern clump B into two regions, B1 and B2, because they show different proper motions (with respect to the central star) as we discuss in the next section.

Although the PSF-subtracted images obtained with ε Sco and Aldebaran show similar clumpy features, the absolute intensity in the clumps C and D, as well as the central compact emission F, turned out to differ significantly, up to 60%. The reason is the aforementioned residual of 2.5% between the PSFs obtained with ε Sco and Aldebaran. This residual represents the difference between two PSFs whose peak is normalized to 1. When the normalized PSFs are scaled to the photospheric flux of Antares, even this small residual leads to a significant difference in the absolute intensity. The 2.5% residual in the PSF is also the reason there are two peaks in the central compact emission in the image obtained with Aldebaran, while there is only

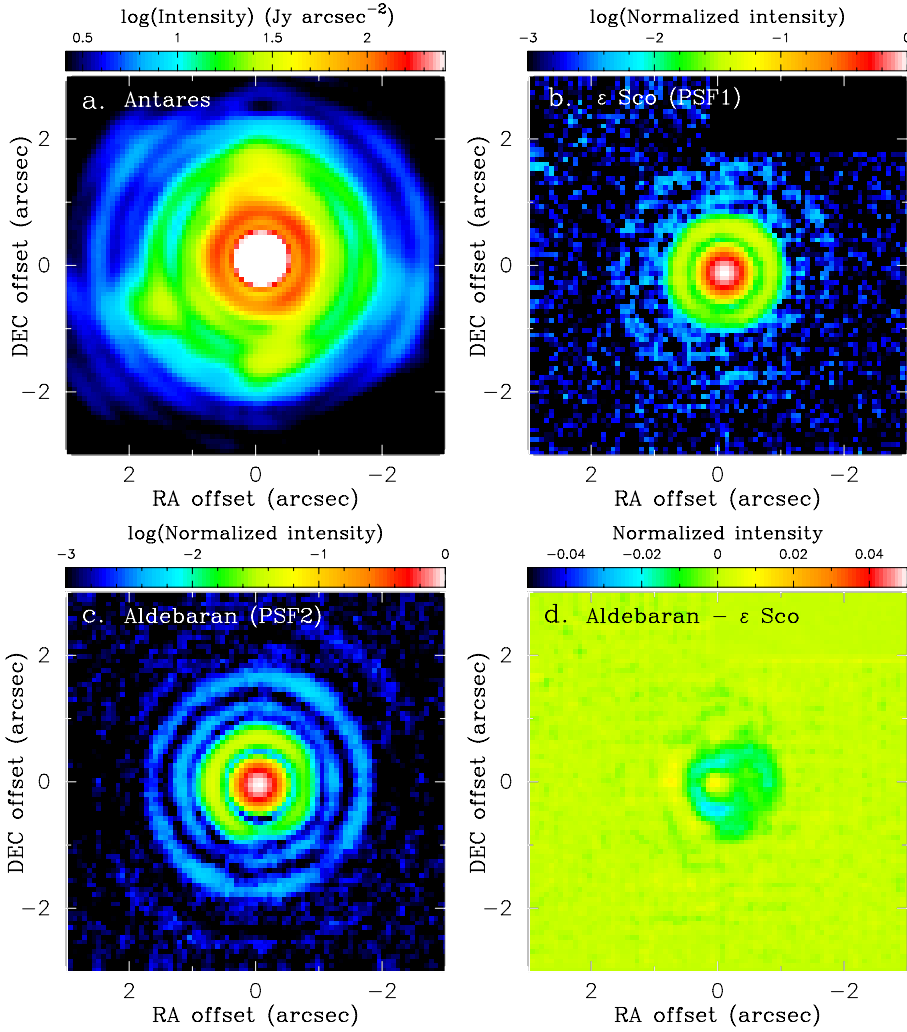


Fig. 4. Enlarged view of the inner $3'' \times 3''$ region of the flux-calibrated Antares image, together with the PSF references ϵ Sco and Aldebaran. North is up, and east to the left. **a)** Flux-calibrated image of Antares. The colors are shown on a logarithmic scale, but the colors in the central region are saturated. **b)** Image of the PSF reference ϵ Sco. The intensity is normalized with the peak intensity. The colors are shown on a logarithmic scale. **c)** Image of the PSF reference Aldebaran, shown in the same manner as in **b)**. **d)** Difference between the images of ϵ Sco and Aldebaran. The colors are shown on a linear scale, ranging from -5% to 5% of the peak intensity of the PSF reference images.

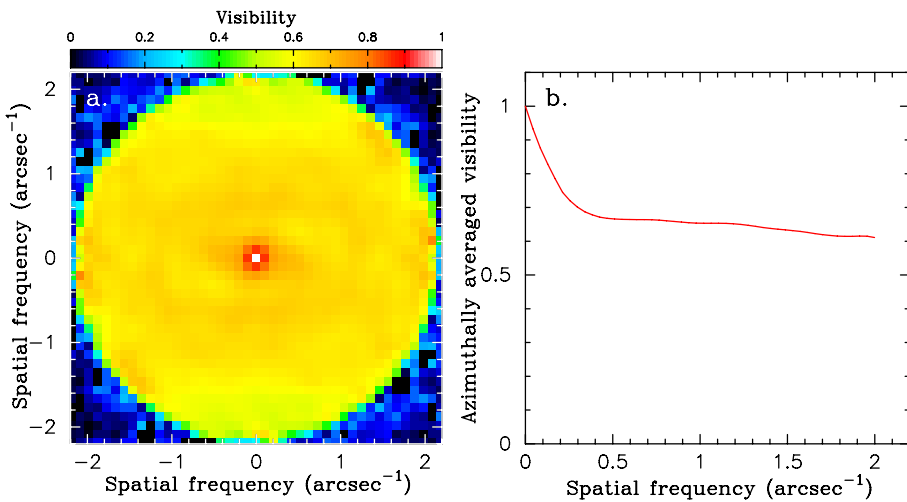


Fig. 5. Calibrated $17.7 \mu\text{m}$ visibility of Antares. **a)** 2D visibility. **b)** Azimuthally averaged visibility.

a single peak in the image obtained with ϵ Sco. It is not clear which is the better PSF – ϵ Sco, which is only 9° away from Antares and was observed close in time but results in the noisy PSF, or Aldebaran, which provides a better signal-to-noise ratio (S/N) but is far away from Antares and was observed on a totally different night. Therefore, we took the mean of the intensities and the fluxes of the clumpy features from both PSF-subtracted images. One half of the difference in the intensity and flux was adopted as the error resulting from the uncertainty in the PSF.

We also added the systematic error in the absolute flux calibration (1135 ± 148 Jy) to the uncertainties of the intensity and flux of the clumps.

The clumps are located at $0'.8\text{--}1'.8$ from the star. At the distance of Antares of 170 pc, these angular distances correspond to 136–306 AU, which in turn translate into 43–96 R_* if a linear radius of $680 R_\odot$ is adopted (Ohnaka et al. 2013). The radius of the compact, central emission corresponds to $27 R_*$ ($= 85$ AU). The intensity of the clumpy features A–E ranges between 23.4

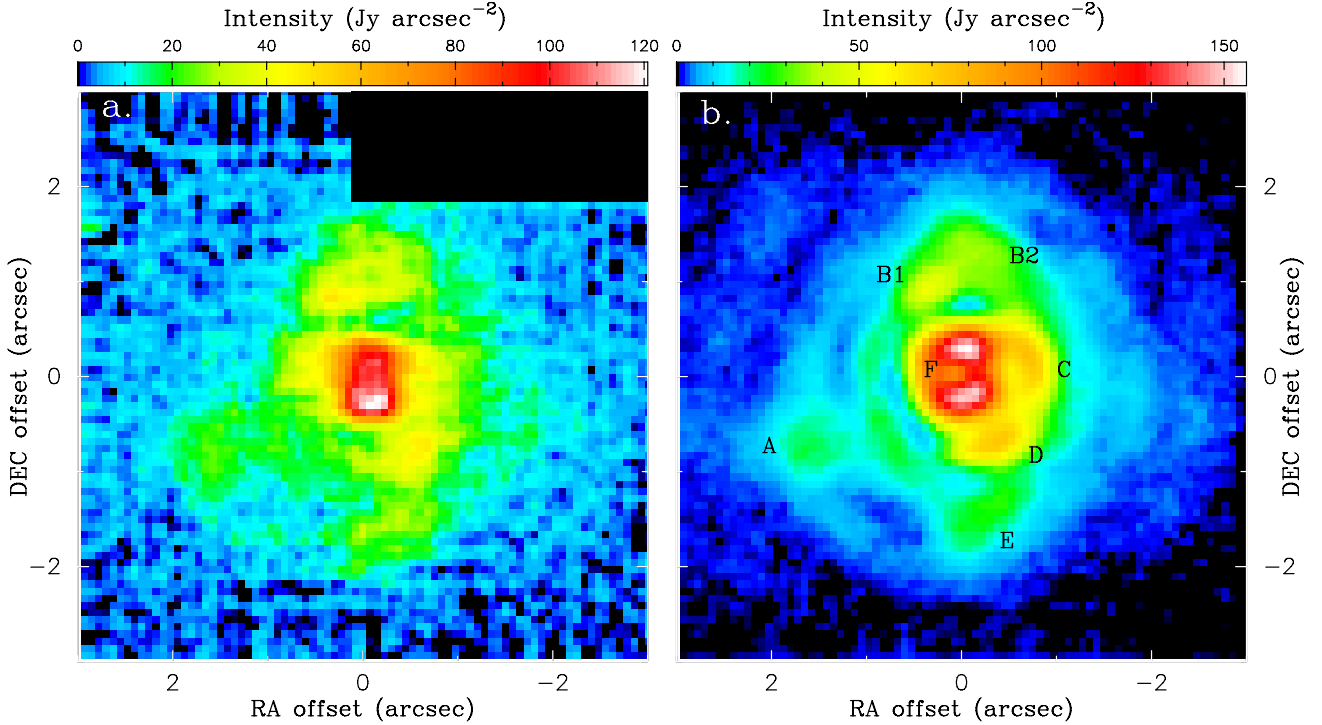


Fig. 6. PSF-subtracted images of Antares obtained with ϵ Sco **a**) and Aldebaran **b**) as the PSF reference. The upper right corner of the image in **a**) is masked because it is affected by a strong detector artefact. North is up, and east to the left.

Table 2. Properties of the dust clouds around Antares.

ID	r (")	r (R_{\star})	PA ($^{\circ}$)	I_{peak} (Jy arcsec^{-2})	Flux (Jy)	T_{d} (K)	M_{d} (M_{\odot})	$r(1998)$ (")	Δr (")	V (km s^{-1})
A	1.8	96	115	23.4 ± 3.9	14.0 ± 2.3	280	5×10^{-9}	1.3	0.5 ± 0.1	34 ± 7
B1	1.0	53	17	50.8 ± 7.8	16.5 ± 2.2	370	3×10^{-9}	0.4	0.6 ± 0.1	40 ± 7
B2	1.3	69	353	36.7 ± 5.4	25.0 ± 3.7	320	5×10^{-9}	1.0	0.2 ± 0.1	13 ± 7
C	0.8	40	289	61.9 ± 22.2	27.7 ± 10.9	430	3×10^{-9}	–	–	–
D	0.8	40	213	60.8 ± 21.0	29.5 ± 9.5	430	3×10^{-9}	–	–	–
E	1.5	78	189	28.9 ± 5.3	16.0 ± 2.4	310	4×10^{-9}	1.0	0.5 ± 0.1	34 ± 7
F	0.5^a	27^a	–	135.0 ± 31.8	87.6 ± 30.2	550	6×10^{-9}	–	–	–

Notes. r : distance from the central star in units of arcseconds and stellar radii. PA: position angle. I_{peak} : peak intensity. Flux: flux integrated over each cloud. T_{d} : dust temperature. M_{d} : dust mass. $r(1998)$: distance from the central star in the $20.8 \mu\text{m}$ image of Marsh et al. (2001) taken in 1998. Δr : angular displacement between 1998 and 2010. V : velocity of the outward motion projected onto the plane of the sky. ^(a) The distance for the clump F actually represents the radius of the inner, compact emission.

and $61.9 \text{ Jy arcsec}^{-2}$, which is 0.9% to 2.4% of the peak intensity of the image before the PSF subtraction. The inner compact emission has a much higher intensity of $135.0 \text{ Jy arcsec}^{-2}$ (at the maximum in the south of the central star), which corresponds to 5.2% of the peak intensity. Table 2 lists the flux integrated over each feature.

There are arc-like features in the PSF-subtracted image obtained with Aldebaran: a semi-circle going through the clump A, a smaller arc at $\sim 1''$ southeast of the star, and a large arc on the western side of the star with a radius of $1''.8$. However, they are presumably residuals of the PSF subtraction. The image quality of the Aldebaran image is still not as good as that of Antares, and therefore, not all Airy rings are detected with sufficient S/N. This can lead to the arc-like residuals in the PSF-subtracted image.

We also performed the deconvolution of the Antares image to cross check the clumpy features seen in the PSF-subtracted images. We used the Lucy-Richardson algorithm (Richardson 1972; Lucy 1974) implemented in the STSDAS package of IRAF, with the Aldebaran image as the PSF. We stopped the deconvolution after five iterations to avoid strong artefacts.

Figure 7a and b show the deconvolved images of the original (i.e., without the PSF subtraction) and PSF-subtracted images of Antares, respectively. The figures confirm the clumps A–E seen in the PSF-subtracted images. The measured integrated flux of the dust clumps in the deconvolved images agrees with the values derived from the PSF-subtracted images. As discussed above, the double peak of the central emission feature F seen in Fig. 7b may be an artefact caused by the uncertainty in the PSF. The central emission feature F is not restored in the deconvolution of the non-PSF-subtracted image. More iterations do not help restore this feature, either. This is probably because the Lucy-Richardson algorithm tends to concentrate surrounding flux onto bright point sources, as Schödel (2010) demonstrates.

4. Discussion

4.1. Physical properties of dust clouds

The modeling of the mid-IR spectrum and interferometric data of Antares by Danchi et al. (1994) and the SED modeling by

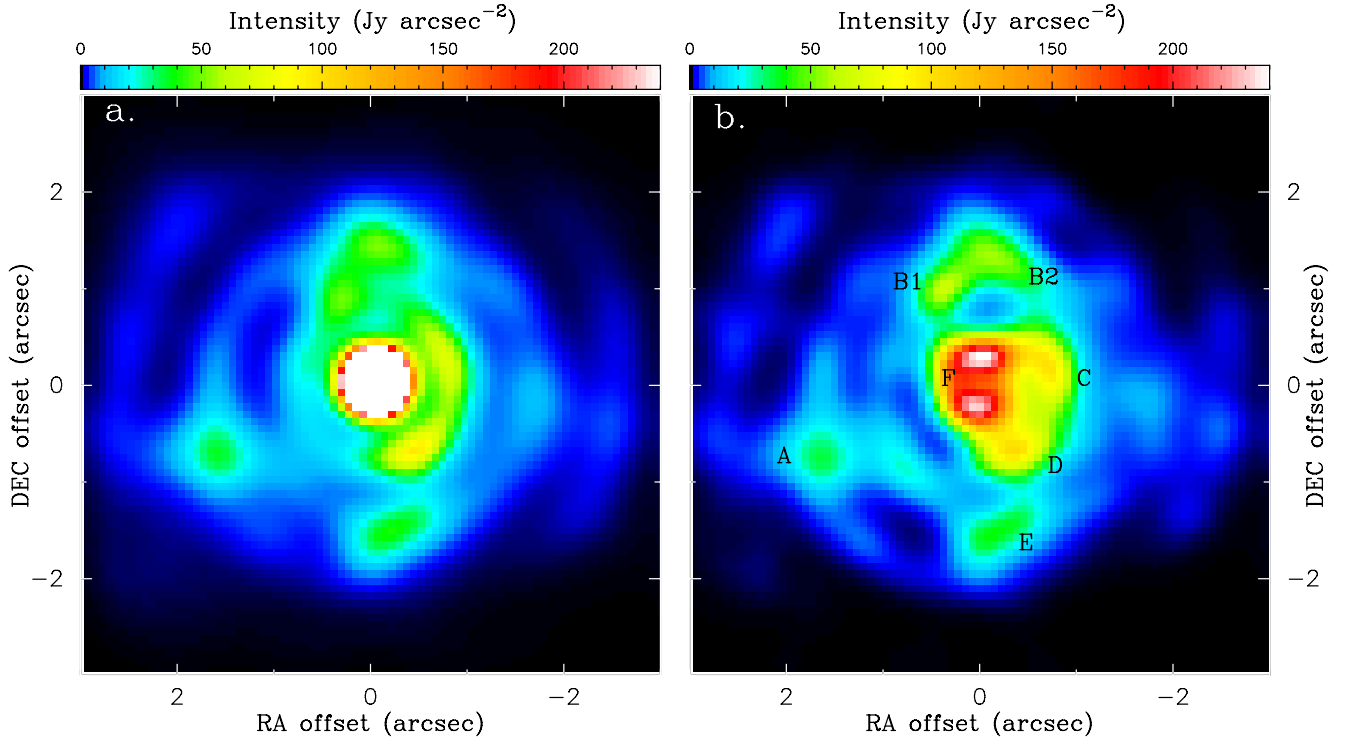


Fig. 7. Deconvolved images of Antares obtained with the Lucy-Richardson algorithm. **a)** Deconvolved image without the PSF subtraction. The colors in the central region are saturated. **b)** Deconvolution of the PSF-subtracted image (obtained with Aldebaran as the PSF). In both cases, the Aldebaran image was used as the PSF for the deconvolution. North is up, and east to the left.

Verhoelst et al. (2009) suggest that the $17.7\ \mu\text{m}$ flux is dominated by dust emission. Harper et al. (2009) report the detection of [Fe II] lines at 17.94 and $24.52\ \mu\text{m}$ in a sample of RSGs including Antares. The former emission line is included in the wavelength range covered by the Q1 filter. Antares was observed only for the 24.52 [Fe II] line and not for the [Fe II] line at $17.94\ \mu\text{m}$. However, Harper et al. (2009) show that the $17.94\ \mu\text{m}$ [Fe II] line forms close to the star at $\sim 1.5 R_\star$, which is unresolved with the spatial resolution of VISIR at $17.7\ \mu\text{m}$. Therefore, the contribution of the [Fe II] line to the clumpy features is likely to be negligible.

The circumstellar dust around Antares is optically thin. For example, Danchi et al. (1994) modeled the mid-IR spectrum ($7\text{--}23\ \mu\text{m}$) and the $11\ \mu\text{m}$ visibility observed for Antares using a spherical shell and derived an $11\ \mu\text{m}$ optical depth of 0.011. We computed the temperature distribution in an optically thin, spherical dust shell with $\tau_{11\mu\text{m}} = 0.011$ using our Monte Carlo code presented in Ohnaka et al. (2006). While the circumstellar envelope of Antares is obviously not spherical, the dust temperature computed in spherical symmetry is a good approximation for an optically thin case. We used the optical properties of silicate presented by Draine & Lee (1984) and a grain size distribution characterized by an exponent of -3.5 between 0.005 and $0.25\ \mu\text{m}$. With these grain properties, the $11\ \mu\text{m}$ optical depth of 0.011 translates into an optical depth of 0.11 at $0.55\ \mu\text{m}$. The central star was approximated by the blackbody of $3700\ \text{K}$, adopting the effective temperature determined by Ohnaka et al. (2013). The density was assumed to decrease as r^{-2} , and we estimated the inner radius of the dust shell from the $12.5\ \mu\text{m}$ image of Antares taken by Marsh et al. (2001). They found a ring with a radius of $0''.3$, which corresponds to $16 R_\star$ with the stellar angular radius of $18.5\ \text{mas}$ measured by Ohnaka et al. (2013). The outer radius of the shell was set to $1.6 \times 10^5 R_\star$.

The dust temperatures derived at the position of the clumps from this model range from 280 to $430\ \text{K}$, as listed in Table 2. The dust temperature at the outer edge of the inner and compact emission F ($27 R_\star$) is $550\ \text{K}$ (dust temperature predicted at the inner boundary of the shell is $780\ \text{K}$). We note that the distance of the individual dust clouds from the star is projected onto the plane of the sky, and therefore the true radial distance from the star can be larger than derived from the VISIR image. This means that the temperatures of the dust clouds derived above are upper limits. However, given that the emission from the dust clouds is significant at $17.7\ \mu\text{m}$, the peak of the blackbody radiation from the dust clouds should be shortward of $17.7\ \mu\text{m}$. This means that the temperatures of the dust clouds would not be lower than $\sim 170\ \text{K}$. Multicolor mid-IR imaging would be useful for reliably determining the temperature of the dust clouds.

We estimated the dust mass (M_d) of the clumps from the dust temperature (T_d) and the flux integrated over each clump (F_ν) by

$$M_d = F_\nu d^2 / (\kappa_\nu B_\nu(T_d)),$$

where d is the distance to Antares, $B_\nu(T_d)$ is the Planck function, and κ_ν the mass absorption coefficient of the dust in units of $\text{cm}^2\ \text{g}^{-1}$. Using the absorption cross section of the astronomical silicate presented by Draine & Lee (1984) and adopting a grain bulk density of $3\ \text{g}\ \text{cm}^{-3}$, we obtain $\kappa_\nu \approx 1000\ \text{cm}^2\ \text{g}^{-1}$ at $17.7\ \mu\text{m}$. The estimated dust mass of the clumps ranges from 3×10^{-9} to $6 \times 10^{-9}\ M_\odot$, as listed in Table 2. Given the aforementioned uncertainty in the dust temperature, the uncertainty in the dust mass amounts to a factor of 2. If we adopt the mass-loss rate of $2 \times 10^{-6}\ M_\odot\ \text{yr}^{-1}$ (Braun et al. 2012) and a gas-to-dust ratio of 100 (Draine & Li 2007), the amount of dust ejected in one year is $2 \times 10^{-8}\ M_\odot\ \text{yr}^{-1}$. This is greater than the derived dust mass of the clumpy clouds by a factor of 3–7, implying the presence of continuous mass loss superimposed on

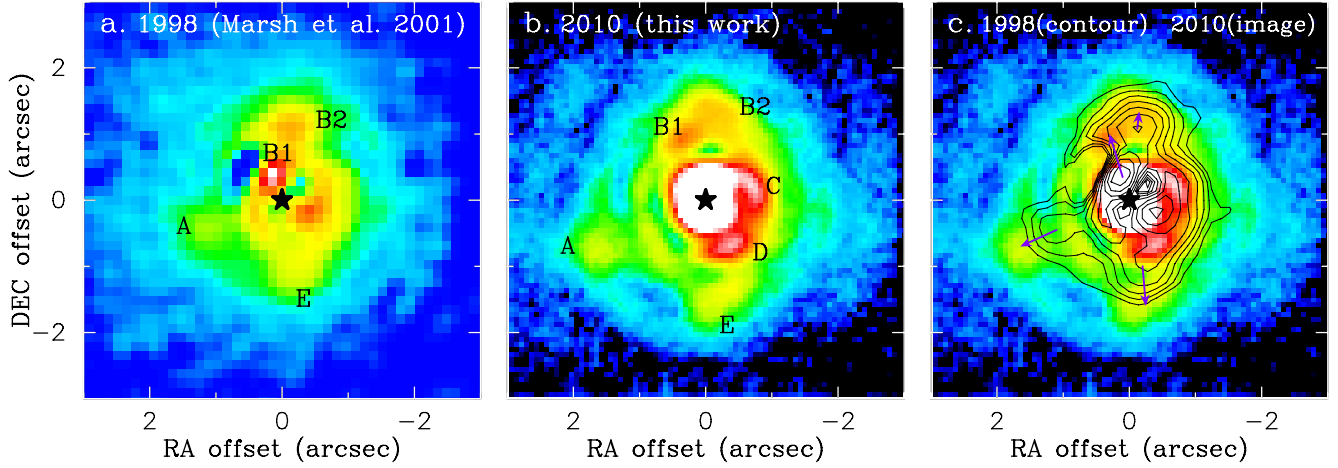


Fig. 8. Temporal evolution of the dust clouds between 1998 and 2010. **a)** PSF-subtracted image of Antares taken at $20.8\ \mu\text{m}$ in 1998 by Marsh et al. (2001). **b)** PSF-subtracted image obtained in 2010 in this work using Aldebaran as the PSF reference. The color in the central core is saturated to show the clumpy structures clearly. **c)** Comparison between the PSF-subtracted images taken in 1998 (contour) and 2010 (image). The outward motions of the clumps A, B1, B2, and E are marked by the arrows. The position of the central star is marked with \star in all panels. North is up, and east to the left.

the clumps. The extended circumstellar envelope (apart from the clumps), which is clearly seen in the azimuthally averaged intensity profile (Fig. 3), corresponds to this continuous mass loss.

4.2. Detection of the outward motions of dust clouds

Marsh et al. (2001) obtained 12.5 and $20.8\ \mu\text{m}$ images of Antares with the Keck Telescope in June 1998, 12 years before our VISIR observation, with a spatial resolution of $0''.48$, which is almost the same as our VISIR image. They detected a ring with a radius of $\sim 0''.3$ and three discrete clumps at a radius of $\sim 1''.2$ from the star. We compared their $20.8\ \mu\text{m}$ image and our $17.7\ \mu\text{m}$ VISIR image to see possible time variations in the clumpy structure of the circumstellar envelope. Figure 8 shows the PSF-subtracted image read off Fig. 1 of Marsh et al. (2001)⁵ and our VISIR image. The figure reveals that the overall structure of the envelope is more extended in our VISIR image than in the Keck image. The wavelengths of the 1998 Keck image and our VISIR image are slightly different ($20.8\ \mu\text{m}$ and $17.7\ \mu\text{m}$, respectively). However, because their wavelength is longer than ours, their image samples colder regions, which are farther away from the star. In other words, if an image had been taken at $17.7\ \mu\text{m}$ in 1998, the ring and the clumpy features would have appeared closer to the star. Therefore, the difference in wavelength is unlikely to be responsible for the time variation of the clumpy features. The inner compact emission is not visible in the Keck image, which suggests that this emission component is newly formed dust ejected after 1998.

Figure 8 allows us to trace the expansion of the individual clumps. As Table 2 summarizes, the dust clumps A, B1, and E have moved over $0''.5$ – $0''.6$ and the clump B2 over $0''.2$ in 12 years. We estimate the uncertainty in the angular displacement to be $\pm 0''.1$, which results from a half of the pixel size of the 1998 Keck image ($0''.138$) and our 2010 VISIR image ($0''.075$). At the distance of 170 pc, the proper motions of $0''.5$ – $0''.6$ and $0''.2$ correspond to distances of $(1.3$ – $1.5) \times 10^{15}$ cm ($=85$ – 102 AU $=27$ – $32 R_{\star}$) and 5.1×10^{14} cm ($=34$ AU $=11 R_{\star}$), respectively, projected onto the plane of the sky. These displacements in 12 years translate into velocities of 34, 40, 13,

and $34\ \text{km s}^{-1}$ for the clumps A, B1, B2, and E, respectively, with an uncertainty of $\pm 7\ \text{km s}^{-1}$ (see Table 2). Because we do not know the 3D positions of the dust clouds, the radial expansion velocity with respect to the star is even higher. On the other hand, we cannot recognize clear outward motions for the clumps C and D. While these clumps may be moving more in parallel to the line of sight, we note that the morphology of the clumps C and D has changed. They appeared as a single clump in 1998, but they clearly appear as two distinct clumps in 2010. Because the spatial resolution of the 1998 Keck image is almost the same as our VISIR image, the difference in the appearance of C and D cannot be attributed to the insufficient spatial resolution of the 1998 image. Perhaps the large clump at $\sim 0''.5$ in the west to southwest seen in the 1998 image may have moved outward, leading to much weaker emission in 2010, and the clumps C and D may be newly formed dust clouds ejected after 1998.

The measured velocity of the clumps A, B1, and E is remarkably higher than the expansion velocity of $17.3 \pm 3.4\ \text{km s}^{-1}$ and $\sim 20\ \text{km s}^{-1}$ derived by Bernat (1977) and Braun et al. (2012), respectively. This implies that the individual clouds may be ejected from the star at different velocities. Baade & Reimers (2007) detected absorption lines blueshifted by 0.5 – $19.9\ \text{km s}^{-1}$ with respect to the star in the UV spectra of Antares, which suggests episodic and/or clumpy mass loss. The analysis of the CO fundamental lines near $4.6\ \mu\text{m}$ in a sample of red giants and supergiants by Bernat (1981) also shows multiple components expanding at different velocities. It cannot be explained simply by the acceleration of material, because there is no correlation between the temperature and expansion velocity of the different components: the faster components do not necessarily show lower temperatures (resulting from being located farther out), as expected from the simple acceleration. These results imply the random nature of the dust cloud ejection mechanism. For example, Wittkowski et al. (2011) propose that the inhomogeneities in the outer atmosphere of Mira stars might be caused by pulsation- and shock-induced chaotic motions. Such chaotic motions may be possible in RSGs as well, although the pulsation amplitude is much smaller than Mira stars. Convective motions and/or magnetohydrodynamical (MHD) processes in the photosphere might also be responsible for the random nature of the ejection velocity of the dust clouds.

⁵ Unfortunately, the original electronic data are no longer available (K. Marsh, priv. comm.).

The absence of the inner emission component F in the Keck image taken in 1998 suggests new dust formation after 1998. If the dust formed in 1998 reached the radius of $0''.5$ in 2010, the expansion velocity is estimated to be 34 km s^{-1} , which agrees with the velocities of the dust clouds A and E derived above. However, given that the expansion velocity can be at least as high as 40 km s^{-1} as in the clump B1, it is possible that the dust formation responsible for the inner component F occurred more recently.

The presence and absence of dust in the inner region of the envelope around Antares has been discussed in previous studies. Based on the $11 \mu\text{m}$ interferometric data, Sutton et al. (1977) showed that dust exists farther than a radius of $0''.2$ from the star. The $11 \mu\text{m}$ imaging of Bloemhof & Danen (1995) confirms the absence of dust within a radius of $\sim 0''.6$ from the star for the data taken in 1985. The PSF-subtracted image obtained at $11 \mu\text{m}$ in 1991 by Danchi et al. (1992) also shows that the intensity at the stellar position is lower than in the surrounding region, suggesting a lower amount of dust near the star. The $11 \mu\text{m}$ interferometric observations and modeling by Danchi et al. (1994) suggest an inner radius of the dust envelope of $\sim 1''$. The mid-IR images taken in 1998 by Marsh et al. (2001) show a ring of dust with a radius of $0''.3$. They estimated that this ring had been ejected 10 to 20 years before their observation in 1998, with the region around the star's position devoid of dust. Then our VISIR image suggests the ejection of newly formed dust after 1998. These results confirm that the dust formation takes place in an episodic manner.

Similar clumpy structures and/or episodic mass loss are suggested for other RSGs as well. The mid-IR imaging of Betelgeuse by Kervella et al. (2011) reveals clumpy structures extending to $\sim 2'' (= 95 R_*)$ from the star. Based on the interferometric measurements at $11 \mu\text{m}$, Tatebe et al. (2007) suggest an episodic ejection of material at 75 km s^{-1} in α Her. Danchi et al. (2001) detected the outward motion of two discrete shells in the dust-enshrouded RSG NML Cyg. Therefore, the mass loss from RSGs – whether optically bright or very dusty – may intrinsically show episodic and clumpy features in addition to continuous outflows.

5. Concluding remarks

We obtained a diffraction-limited image of the RSG Antares at $17.7 \mu\text{m}$ with a spatial resolution of $0''.5$. The image shows six clumpy dust clouds at $0''.8$ – $1''.8$ away from the star, as well as the inner compact emission with a radius of $0''.5$. The clumpy dust clouds have peak intensities of 0.9% to 2.4% of the central star, while the inner emission has a much higher intensity of 5.2% of the central star. We set upper limits of 280–550 K on the temperature in the dust clouds. The estimated dust mass of the individual clouds is $(3\text{--}6) \times 10^{-9} M_{\odot}$, which is less than the amount of dust ejected in one year by a factor of 3–7. This means that the mass loss from Antares consists of the ejection of clumpy dust clouds and a continuous outflow.

We detected the outward motions of the dust clouds by comparing with the $20.8 \mu\text{m}$ image taken in 1998 with the Keck telescope. The measured proper motions amount to $0''.2$ – $0''.6$ in 12 years. The expansion velocity of the dust clouds (projected onto the plane of the sky) is 13 – 40 km s^{-1} . The inner compact

emission is not seen in the Keck image taken in 1998, suggesting that newly formed dust was ejected between 1998 and 2010. If we adopt the radial expansion velocity of 34 km s^{-1} for the inner component, it must have been ejected in 1998. However, given that we derived a velocity as high as 40 km s^{-1} in one cloud, it is also possible that the new dust formation occurred later than 1998. Spatially resolved spectroscopy of the individual dust clouds would be useful for probing their kinematics and obtaining a 3D picture of the clumpy circumstellar envelope. The outward velocities of the dust clumps cannot be explained by a simple accelerating outflow, implying the random nature of the dust cloud ejection mechanism.

Acknowledgements. We thank the ESO VLT team for supporting our VISIR observations. This research made use of the SIMBAD database, operated at the CDS, Strasbourg, France.

References

- Baade, R., & Reimers, D. 2007, *A&A*, 474, 229
 Bernat, A. P. 1977, *ApJ*, 213, 756
 Bernat, A. P. 1981, *ApJ*, 246, 184
 Bloemhof, E. E., & Danen, R. M. 1995, *ApJ*, 440, L93
 Braun, K., Baade, R., Reimers, D., & Hagen, H.-J. 2012, *A&A*, 546, A3
 Cruzalèbes, P., Lopez, B., Bester, M., Gendron, E., & Sams, B. 1998, *A&A*, 338, 132
 Danchi, W. C., Degiacomi, C. G., Bester, M., & Greenhill, L. J. 1992, *Proc. ESO Conference on High-Resolution Imaging by Interferometry II. Ground-Based Interferometry at Visible and Infrared Wavelengths*, eds., J. M. Beckers, & F. Merkle (Garching bei München: European Southern Observatory), 21
 Danchi, W. C., Bester, M., Degiacomi, C. G., Greenhill, L. J., & Townes, C. H. 1994, *AJ*, 107, 1469
 Danchi, W. C., Green, W. H., Hale, D. D. S., et al. 2001, *ApJ*, 555, 405
 de Wit, W. J., Oudmaijer, R. D., Fujiyoshi, T., et al. 2008, *ApJ*, 685, L75
 de Wit, W. J., Hoare, M. G., Fujiyoshi, T., et al. 2009, *A&A*, 494, 157
 Doucet, C., Habart, E., Pantin, E., et al. 2007, *A&A*, 470, 625
 Draine, B. T., & Lee, H. M. 1984, *ApJ*, 285, 89
 Draine, B. T., & Li, A. 2007, *ApJ*, 657, 810
 Harper, G. M., Richter, M. J., Ryde, N., et al. 2009, *ApJ*, 701, 1464
 Hinz, P. M., Angel, J. R. P., Hoffmann, W. F., et al. 1998, *Nature*, 395, 251
 Humphreys, R. M., Helton, L. A., & Jones, T. J. 2007, *AJ*, 133, 2716
 Kastner, J. H., & Weintraub, D. A. 1998, *AJ*, 115, 1592
 Kervella, P., & Domiciano de Souza, A. 2007, *A&A*, 474, L49
 Kervella, P., Verhoelst, T., Ridgway, S. T. et al. 2009, *A&A*, 504, 115
 Kervella, P., Perrin, G., Chiavassa, A., et al. 2011, *A&A*, 531, A117
 Lagage, P.O., Pel, J. W., Authier, M., et al. 2004, *The Messenger*, 117, 12
 Lobel, A., & Dupree, A. K. 2001, *ApJ*, 558, 815
 Lucy, L. B. 1974, *AJ*, 79, 745
 Marsh, K. A., Bloemhof, E. E., Koerner, D. W., & Ressler, M. E. 2001, *ApJ*, 548, 861
 Monnier, J. D., Millan-Gabet, R., Tuthill, P. G., et al. 2004, *ApJ*, 605, 436
 Ohnaka, K., Driebe, T., Hofmann, K.-H., et al. 2006, *A&A*, 445, 1015
 Ohnaka, K., Driebe, T., Hofmann, K.-H., Weigelt, G., & Wittkowski, M. 2008, *A&A*, 484, 371
 Ohnaka, K., Hofmann, K.-H., Benisty, M., et al. 2009, *A&A*, 503, 183
 Ohnaka, K., Weigelt, G., Millour, F., et al. 2011, *A&A*, 529, A163
 Ohnaka, K., Hofmann, K.-H., Schertl, D., et al. 2013, *A&A*, 555, A24
 Reimers, D., Hagen, H.-J., Baade, R., & Braun, K. 2008, *A&A*, 491, 229
 Richardson, W. H. 1972, *J. Opt. Soc. Am.*, 62, 55
 Schödel, R. 2010, *A&A*, 509, A58
 Sutton, E. C., Storey, W. V., Betz, A. L., & Townes, C. H. 1977, *ApJ*, 217, L97
 Tatebe, K., Hale, D. D. S., Wishnow, E. H., & Townes, C. H. 2007, *ApJ*, 658, L103
 van Leeuwen, F. 2007, *A&A*, 474, 653
 Verhoelst, T., Van der Zypem, N., Hony, S., et al. 2009, *A&A*, 498, 127
 Wittkowski, M., Langer, N., & Weigelt, G. 1998, *A&A*, 340, L39
 Wittkowski, M., Boboltz, D. A., Ireland, M., et al. 2011, *A&A*, 532, L7